CARDIFF UNIVERSITY
PRIFYSGOL CAERDYDD

ORCA – Online Research @ Cardiff

This is an Open Access document downloaded from ORCA, Cardiff University's institutional repository:https://orca.cardiff.ac.uk/id/eprint/95940/

This is the author's version of a work that was submitted to / accepted for publication.

Citation for final published version:

Fang, Huihuang, Zheng, Jianwei, Luo, Xiaolin, Du, Junmou, Roldan Martinez, Alberto , Leoni, Stefano and Yuan, Youzhu 2017. Product tunable behavior of carbon nanotubes-supported Ni?Fe catalysts for guaiacol hydrodeoxygenation. Applied Catalysis A: General 529 , pp. 20-31. 10.1016/j.apcata.2016.10.011

Publishers page: http://dx.doi.org/10.1016/j.apcata.2016.10.011

Please note:
Changes made as a result of publishing processes such as copy-editing, formatting and page numbers may not be reflected in this version. For the definitive version of this publication, please refer to the published source. You are advised to consult the publisher's version if you wish to cite this paper.

This version is being made available in accordance with publisher policies. See http://orca.cf.ac.uk/policies.html for usage policies. Copyright and moral rights for publications made available in ORCA are retained by the copyright holders.

Product tunable behavior of carbon nanotubes-supported Ni–Fe catalysts for guaiacol hydrodeoxygenation

Huihuang Fang[1], Jianwei Zheng[1], Xiaolin Luo[1] Junmou Du[1], Alberto Roldan[2], Stefano Leoni[2]*, Youzhu Yuan[1]*

[1] *State Key Laboratory of Physical Chemistry of Solid Surfaces, National Engineering Laboratory for Green Chemical Productions of Alcohols-Ethers-Esters and iChEM, College of Chemistry and Chemical Engineering, Xiamen University, Xiamen, 361005, China*

[2] *School of Chemistry, Cardiff University, Main Building, Park Place, Cardiff, CF10 3AT, United Kingdom*

* To whom correspondence should be addressed. E-mail: yzyuan@xmu.edu.cn, LeoniS@cardiff.ac.uk

Abstract

Bimetallic Ni–Fe nanoparticles supported on carbon nanotubes (CNTs) were prepared and evaluated for catalytic hydrodeoxygenation (HDO) of guaiacol, which is a model lignin-derived compound. Appropriate combination of Ni and Fe demonstrated high activity and significantly enhanced selectivity to cyclohexane and phenol, whereas monometallic Ni and Fe catalysts displayed poor activities or selectivities. The tunable selectivity of guaiacol HDO was found to be dependent on Ni/Fe atomic ratios. Cyclohexane and phenol are major products over the Ni_5–Fe_1/CNT and Ni_1–Fe_5/CNT catalysts, respectively. Characterization results confirmed that Ni–Fe alloys were formed and elicited synergistic effects on the HDO performance. The selectivity-switchable performance of Ni–Fe/CNT may be due to the synergism between Ni domains, where H_2 could be easily activated, and Fe domains, which exhibited strong oxophilicity. Deactivation was observed over the monometallic catalyst which may be ascribed to the agglomeration of active nanoparticles. Metallic size effect on the HDO reaction was further investigated using monometallic Ni/CNT, Fe/CNT and bimetallic Ni–Fe/CNT catalysts.

Keywords: Ni–Fe catalyst; hydrodeoxygenation; guaiacol; cyclohexane; phenol

1. Introduction

Renewable feedstocks, such as lignocellulose, have gained considerable attention for sustainable production of fuel and chemicals because of the limited availability and passive effect of fossil fuels [1-5]. Lignin, an amorphous tri-dimensional biopolymer containing abundant methoxylated propyl phenol units, is the second most important compound in lignocellulosic biomass (15%–20%) [6]. In contrast to cellulose and hemicellulose, lignin is the most similar to petroleum in structure and composition, which is industrially available from biomass-to-ethanol processes and other biorefineries [7]. Generally, lignocellulosic biomass is directly converted into aromatics and bio-oils through a traditional method known as rapid pyrolysis [3]. However, the methoxylated propyl phenol unit contains numerous C_{aryl}–OCH_3, C_{aryl}–OH, and C_{aryl}–OR bonds; as such, the pyrolysis product is comprised high amounts of oxygen and oxo-functionalized groups than commercial fuel and thus presents limited applications [8]. In addition, lignin-derived phenolic compounds are highly reactive during fast pyrolysis, which leads to the formation of oligomers and deactivation of catalysts [9,10]. Therefore, upgrading of bio-oils through hydrodeoxygenation (HDO) with hydrogen consumption is valuable [11].

Guaiacol, a model compound of lignin-derived bio-oils, contains two types of O-containing functional groups (C_{aryl}–OCH_3 and C_{aryl}–OH), which are characteristic components of lignin-derived compounds [12,13]. Hence, the catalytic hydrogenolysis and HDO of guaiacol have gained increased research attention to elucidate the roles of catalysts and identify their industrial applications.

Metal sulfides, such as MoS_2, NiMoS, and CoMoS, as well as supported noble metals,

such as Ru, Pt, and Pd which are widely used in hydrodesulfurization, are also applied in HDO because of their similarity to S and O [14,15]. Metal sulfides exhibit satisfactory activities but deactivate rapidly, especially during the formation of water as the byproduct [2,6,16]. The activated sulfide form of catalysts is maintained through continuous addition of S to the reactant stream, causing serious negative effects on downstream processes [17,18]. Using noble metals for HDO of guaiacol could avoid these problems [11,13,19,20]. Gates et al. [21,22] used Pt catalysts for HDO of lignin-derived species and reported that hydrogenolysis of C–O bonds is the most kinetically available route that does not remove oxygen. Varma et al. [23] systematically surveyed the HDO of guaiacol on noble metal catalysts; the developed Pt/C catalysts showed superior activity at the optimal operating temperature of 573 K. Supported noble metal catalysts demonstrate satisfactory activity but have limited applications because of the high cost of noble metals. Hence, novel metal catalysts such as non-noble metallic catalysts should be developed for economic viability and engineering aspects.

Ni is cheaper than noble metals and shows high activity in hydrogenation reactions; as such, this element is widely used as a metallic catalyst [24-28]. Zhao et al. [27] reported that Ni/HZSM exerts synergistic effects on HDO and C–O bond cleavage of substituted phenols. Ma et al. [24] investigated Ni-based catalysts supported by mixed oxides and found that Ni/TiO_2–ZrO_2 displayed the optimal performance, with a cyclohexane yield of 86.4% in the solvent decalin at 573 K and 4.0 MPa H_2. Recently, Dongil et al. [29] obtained tunable selectivities of cyclohexane and cyclohexene over CNTs supported Ni nanoparticles inside and outside. On the other hand, several reports also indicated that Fe was active in selective

cleavage of aryl C–O bonds [25,26]. Olcese et al. [26] found that the Fe/SiO_2 catalyst demonstrated efficient in hydrogenolysis for guaiacol HDO. However, these mono-metallic catalysts exhibit inherent low activity and poor stability. In this regard, a second metal is added to form bimetallic nanoparticles, such as Ni–Cu, Pt–Sn and Pd–Fe, which can remarkably promote catalytic properties as a result of geometric and electronic effects [28,30]. Ardiyanti et al. [28] found that bimetallic catalysts promoted higher HDO activity than the mono-metallic Ni and Cu catalysts for hydrotreatment of anisole over Ni–Cu catalysts; Sun et al. [30] reported that Pd–Fe/C bimetallic catalyst benefit the HDO of guaiacol to benzene with 83.2% yield at 723 K.

In this study, bimetallic Ni–Fe catalysts supported on carbon nanotubes (CNTs) were prepared and firstly applied to investigate the relationship between the bimetallic structure and the HDO performance of guaiacol, particularly selectivity. In all cases, CNTs are used as carriers due to their special electrical properties, hydrogen spillover, and chemical stability, which have triggered wide research interest [31,32]. Product distribution was correlated with the amounts of Ni and Fe. The synthesized catalysts displayed tunable selectivity to cyclohexane or phenol at Ni/Fe ratio of 5:1 or 1:5, respectively. Further experiments including X-ray powder diffraction (XRD), H_2-temperature-programmed reduction (H_2-TPR), transmission electron microscopy (TEM), X-ray photoelectron spectroscopy (XPS), high-sensitivity low-energy ion scattering spectroscopy (HS-LEIS), Raman spectroscopy analyses, and computational modelling were performed to elucidate the interaction between Ni and Fe. The results revealed the key role of different metals on the HDO pathway and confirmed the synergistic effect of Ni–Fe alloy nanoparticles, in

which the Ni domains demonstrated high ability to activate H_2 and the Fe domain displayed strong oxophilicity. Meanwhile, deactivation of monometallic catalysts was observed which may be ascribed to the agglomeration of nanoparticles. Size effects of the catalysts were further investigated.

2. Experimental

2.1. Catalyst preparation

CNTs with 97% purity were obtained from Shenzhen Nanotech Port Co., Ltd. The purchased CNTs contain parallel multiwall structures with a diameter of 20–40 nm. Before catalyst preparation, the CNTs as received were pretreated in concentrated HNO_3 (68 wt%) at 353 K for 16 h under reflux conditions to remove residual catalysts and amorphous C. The treated CNTs were thoroughly washed with a large quantity of deionized water until the pH became neutral and then dried overnight.

Ni–Fe bimetallic catalysts were prepared through co-impregnation using aqueous solutions of $Ni(NO_3)_2{\cdot}6H_2O$ and $Fe(NO_3)_3{\cdot}9H_2O$. The total loading weight of metal was maintained at 7 wt%, and the Ni/Fe atomic ratio was accordingly adjusted. Typically, 1 g of CNT was added to 30 mL of distilled water containing required amounts of $Ni(NO_3)_2{\cdot}6H_2O$ and $Fe(NO_3)_3{\cdot}9H_2O$ with vigorous stirring for 6 h. Then, the aqueous solution removed the excess solvent by evaporation to keep an incipient wetness liquid/solid ratio of 1 mL/g. After impregnation for 12 h at room temperature and solvent removal by evaporation, the mixture was dried at 373 K overnight. All dry solids were calcined for 4 h at 573 K with a heating ramp of 2 K/min in the atmosphere. The catalysts were reduced by 5% H_2/95% N_2

(25 mL/min) for 4 h prior to the reaction. The bimetallic catalyst was denoted as Ni_x–Fe_y/CNT, where *x* and *y* represent the atomic ratios of Ni and Fe, respectively. Monometallic catalysts, namely, Ni/CNT and Fe/CNT, were prepared using the same method.

2.2. Catalyst characterization

Ni and Fe contents of the catalysts were determined through inductively coupled plasma optical emission spectrometry (ICP-OES) using a Thermo Elemental IRIS Intrepid II XSP. The samples were pretreated with aqua regia at 353 K for 1 h, and the remaining solution was heated to remove the solvent. The residues were diluted with 5% HNO_3 and filtered in a 50 mL volumetric flask before measurement.

A nitrogen sorption isotherm was determined at 77 K by using a Micromeritics TriStar II 3020 porosimetry analyzer. The sample was degassed at 573 K for 3 h prior to the measurements. Specific surface area was determined through Brunauer–Emmett–Teller (BET) method. Pore size and average pore diameter distributions were calculated from the desorption isotherm branch according to the Barret–Joyner–Halenda method. The total pore volume of the samples depended on the adsorbed N volume at a relative pressure of approximately 0.99.

Powder XRD patterns were obtained on a Phillips PANalytical X'pert Pro diffractometer equipped with a graphite monochromator and Cu–K_α radiation (40 kV and 30 mA) at scanning 2θ from 10° to 90°. The obtained diffraction data were identified and compared with reference patterns in the JCPDS database.

H_2-TPR spectra were determined using a Micromeritics AutoChem II 2920 chemisorption analyzer. The sample was pretreated in Ar (30 mL/min) at 573 K for 30 min and then cooled to room temperature. The reducing gas (5% H_2/95% N_2) was then flowed through the sample at a rate of 30 mL/min, and the ambient temperature was raised to 1173 K at a rate of 10 K/min. A thermal conductivity detector was used to monitor H_2 consumption.

TEM studies were performed using an electron microscope (Philips Analytical FEI Tecnai 20) operated at an acceleration voltage of 300 kV. The samples for TEM analysis were ultrasonically dispersed in ethanol. Drops of the suspension were deposited on copper grids coated with C films.

XPS spectra were recorded on an Omicron Sphera II photoelectron spectrometer equipped with an Al–K_α X-ray radiation source ($h\nu$ = 1486.6 eV). The machine is connected to HS-LEIS, in which measurement was performed by IONTOF Qtac100 using $20Ne^+$ (5 keV) as Fe source. The scattering angle was 145°. The sample was treated in an *in situ* chamber with 5% H_2−95% N_2 at 673 K for 4 h before the measurement. All measurements were performed in a system with combined elevated pressure reaction cell and ultrahigh vacuum (UHV). Sample preparation and characterization were conducted in the primary UHV chamber (base pressure, 7×10^{-9} Torr).

Raman spectra were obtained using a Renishaw inVia Raman microscope equipped with an Ar ion laser at an excitation wavelength of 514 nm and a laser source intensity of 10%.

2.3. Catalytic testing

The catalytic reactions for HDO were performed on a conventional fixed-bed flow reactor equipped with an auto-sampling system (Figure S1). Briefly, 100 mg of the as-calcined catalyst was placed in the center of the reaction tube and sandwiched by quartz powders. Prior to the experiment, the catalyst precursor was reduced under 5% H_2–95% N_2 at 673 K for 240 min at a ramping rate of 3 K/min. After cooling the catalyst bed to the reaction temperature, pure H_2 was fed into the reactor and held at 3.0 MPa. For the HDO reaction, pure guaiacol was introduced to the reactor by flowing H_2 gas by using a Series III digital HPLC pump (Scientific Systems, Inc.). The catalysts were stabilized for 2 h after the feed was introduced. The product line was heated at 583 K before cold trap to avoid condensation of liquid products. An Agilent 7890A gas chromatograph (GC), equipped with an auto-sampling valve, DB-Wax (30 m × 0.32 mm × 0.25 μm) capillary column, and flame ionization detector was used to analyze the products. The mixture collected through condensation was analyzed by an Agilent 7890GC-5975MS system. After the condensation of the products, the dry gas was conveyed into a GC 2060 with a TDX column for analysis of gas products (CO, CH_4, CO_2, and H_2O). The response factors of guaiacol and products were determined using pure compounds with known concentrations. The carbon balance is about 95% ± 2%, unless otherwise noted. Guaiacol conversion (X_{GUA}), selectivity of C6 ring products (S_{C6i}) and selectivity of C1 products (S_{C1i}) were calculated as follows:

$$X_{GUA} = \frac{(\text{moles of GUA})_{in} - (\text{moles of GUA})_{out}}{(\text{moles of GUA})_{in}} \times 100\%$$

$$S_{C6i} = \frac{\text{moles of ring product i}}{\text{the sum moles of guaiacol consumed}} \times 100\%$$

$$S_{C1i} = \frac{\text{moles of produced methane or methanol}}{\text{the sum moles of guaiacol consumed}} \times 100\%$$

Unless otherwise mentioned, the reported conversion and selectivity were obtained after the reaction proceeded for 2 h when the ready state was reached. In some cases, the total selectivity of C1 products is less than 100% because of the transalkylation reaction or the formation of coke.

2.4. Computational modelling

The catalyst surface was simulated with a periodic slab model of Ni exposing the most stable surface (111). Each slab represents a *p(3x3)* cell with an area of 44.6478 $Å^2$ and five atomic layers where the top two are fully relaxed while the bottom surface remain fix at the optimized interatomic distance simulating the bulk. A vacuum of 15 Å avoids the interactions between the slab and its images. As a doped model, we replaced three Ni from the pristine surface with Fe. We studied two different configurations and found that an alternating distributions of Fe atoms is 0.19 eV more stable than Fe agglomeration. To obtain the properties of isolated molecules, we placed them in the center of a 19x20x21 $Å^3$ simulation cell to avoid lateral interactions, with broken symmetry, and using the same criteria of convergence as for the metallic surfaces.

All calculations were carried out with the density-functional theory-D2 (DFT-D2) as implemented in the Vienna ab initio simulation package (VASP) [33,34]. The Kohn-Sham valence states were expanded in a plane-wave basis set with a cut off at 450 eV for the

kinetic energy [35]. The electron exchange-correlation was denoted by the generalized gradient approximation (GGA) with the Perdew-Burke-Ernzerhof revised for solids (PBEsol) [36]. All the calculations include long-range dispersion correction Grimme approach [37], which is an improvement on standard DFT [38-40]. A Monkhorst-Pack grid of 5x5x1 k-points was used to evaluate the wavefunctions which ensures the electronic and ionic convergence [41]. The systems were considered converged when the force on each ion dropped below 0.01 eV/Å and the energy threshold defining self-consistency of the electron density was set to 10^{-5} eV.

We have calculated the energy variations (ΔE) along the reaction pathway according to Eq. 1, E_{System} being the energy of the slab and adsorbates, E_{Surf} the energy of the naked slab, E_{Gua} and $n.E_{H2}$ the energy of the isolated guaiacol and H_2 molecules.

$$E_B = E_{System} - \left(E_{Surf} + E_{Gua} + n \cdot E_{H_2}\right) \qquad \text{Eq. } \mathbf{1}$$

3. Results and discussion

3.1. Catalyst characterization

A series of supported Ni–Fe bimetallic catalysts were prepared with a fixed total metal loading (7%) but varied Ni/Fe atomic ratios. The physicochemical properties of the catalysts are summarized in Table 1. The ICP–OES results show that actual metal loading is similar to the preset values in the preparation. The BET surface area of CNTs is approximately 147 $m^2\ g^{-1}$, and all surface areas of catalysts approximate those of CNTs after loading with metals.

The XRD patterns of the samples after reduced under 5% H_2/95% N_2 at 673 K for 4 h

are shown in Figures 1 and S2. Distinct diffraction peaks of the metal Ni species were observed at 2θ = 44.50°, 51.60°, 76.08°, which correspond to the (111), (200), and (220) reflections of the Ni phase (PDF 00-001-1258). No significant diffraction peaks of Fe^0 species are found, which is due to reduced Fe^0 species are well dispersed on the surface of catalyst. The diffraction lines of the Ni–Fe alloy are similar to those of monometallic Ni and Fe, which exhibit similar face-centered cubic structures and lattice constants. The peak position corresponding to (111) are shifted to lower angles (from 44.50° to 43.90°) with increasing Fe content, indicating the formation of Ni–Fe alloy. This result is consistent with previously reported results [42,43]. In addition, diffraction peaks emerge at 2θ = 44.28°, 51.53°, 75.87° for bimetallic catalysts, which is ascribed to the diffractions of Fe_1Ni_3 alloy phase (PDF 00-038-0419). With increasing Fe content, diffraction peaks belonging to Fe_3O_4 (2θ = 30.06°, 35.45°; PDF 00-001-1111) appeared because of incomplete reduction of iron oxide at 673 K. The XRD patterns of samples after reduced at 773 and 873 K are shown in Figures S3 and S4, respectively. The diffraction peak at 2θ = 44.64° belonging to Fe^0 species appeared in the Fe/CNT sample while the Fe_3O_4 phase disappeared, which suggested that iron oxides could be reduced completely at 873 K.

The average diameters of nanoparticles reduced at 673 K, 773 K, and 873 K based on the Scherrer equation are summarized in Table 1, and Table 2, respectively. Crystallite size decreased with increase amount of Fe, suggesting that Fe promoted the dispersion of metallic Ni. Additionally, an increase of sample reduction temperatures ~~with increase of reduction temperature of samples~~ increased the nanoparticle size evidently. Figure S5-a–f shows the TEM images and nanoparticle size distribution of catalysts freshly reduced at 673

K containing varied Ni/Fe atomic ratios. The mean nanoparticle sizes of monometallic Ni/CNT and Fe/CNT are 8.7 and 5.1 nm, respectively. The average particle sizes of bimetallic particles are smaller than that of Ni/CNT and decreased (7.3, 6.9, 6.2, and 5.3 nm at a Ni/Fe ratio of 5:1, 2:1, 1:1, and 1:5, respectively) with decreasing Ni/Fe atomic ratio. Both the XRD and TEM results indicate that Fe species is beneficial for Ni dispersion.

Ni–Fe/CNT was characterized using HR-TEM and STEM-EDS analyses to observe distribution of Ni and Fe in bimetallic catalysts (Figure 2). The representative HRTEM image (Figure 2-a) shows a 0.205 nm distance between the corresponding lattice fringes, and this distance is consistent with the lattice spacing of Ni–Fe alloy [46]. The results of nanoscale elemental STEM–EDS mapping and linear scanning analyses are shown in Figure 2-b–c. Ni was well distributed throughout the Fe domain, indicating that Ni and Fe are homogeneous distributed along the bimetallic particles. Ni species displayed improved distribution than Fe possibly because some Fe_3O_4 particles were not reduced completely. The linear scanning analysis also confirmed the mapping results. The distribution of Ni is similar to that of Fe in an individual particle, and the formation of Ni–Fe alloy in the Fe domain was verified. These results are consistent with the XRD patterns and the computational models.

In situ XPS and HS-LEIS analyses were performed to determine the structure and electronic properties of Ni–Fe nanoparticles. The Ni 2p and Fe 2p spectra of Fe/CNT, Ni/CNT, Ni_2–Fe_1/CNT, and Ni_5–Fe_1/CNT are displayed in Figure 3. Data on XPS curve fitting are summarized in Table S1. All XPS peaks were identified according to published data and an on-line database (www.lasurface.com). In contrast to those of bimetallic

Ni–Fe/CNT samples, the Fe 2p spectra of Fe/CNT [Figure 3(A)-a] showed a binding energy of Fe $2p_{3/2}$ at 711.0 eV and that of Fe $2p_{1/2}$ at 724.0 eV, a typical characteristic of Fe^{3+}. To check the rationality of peak-fitting we executed the curve-fitting by fitting two peaks at 707.3 and 709.0 eV. The results became worse, indicating that only Fe^{3+} existed on the surface of Fe/CNT sample. Hence, Fe species supported on CNTs were hardly reduced at 673 K within 4 h. Nevertheless, the results for bimetallic NiFe/CNT samples revealed that the Fe 2p spectra evidently changed [Figure 3(A)-b–c]. Three peaks of the binding energy of Fe $2p_{3/2}$ were identified at 707.3, 709.0, and 711.0 eV for Ni_2–Fe_1/CNT and Ni_5–Fe_1/CNT. In addition, a binding energy of approximately 715.0 eV was ascribed to the satellite peak of Fe^{2+} species, and is commonly observed in Fe^{2+} compounds. The original peaks at 707.3 and 709.0 eV are ascribed to the binding energy of Fe^0 and Fe^{2+}, respectively; this finding indicates that some Fe^{3+} species were reduced into FeO and Fe^0 in the presence of Ni species. Thus, Ni addition promoted the reduction of iron oxide. Similarly, XPS peaks of Ni were observed at 853.2, 854.7, and 856.7 eV for monometallic Ni/CNT [Figure 3(B)-a]; these peaks are attributed to Ni^0, Ni^{2+}, and Ni^{3+}, respectively. These results indicated that a certain proportion of nickel oxides were still exist even under the reduction conditions, in agreement with previous reports [44,45]. Figure 3(B)-b–c shows the results for Ni_2–Fe_1/CNT, and Ni_5–Fe_1/CNT. The appearance of Ni^0 revealed that Ni species were more easily reduced than Fe species under similar reduction treatments.

Ni and Fe concentrations were calculated by peak fitting (Table S1). Bimetallic Ni–Fe/CNT catalysts displayed higher concentrations of Fe^0 and Ni^0 than those in the monometallic Fe/CNT or Ni/CNT catalysts. Values increased with increasing Fe content.

The Ni concentration of bimetallic NiFe/CNT samples demonstrated improved reducibility than that of monometallic Ni/CNT. The introduction of Fe did not inhibit but promoted Ni reduction. This phenomenon could be due to easier reduction of highly dispersed Ni species than monometallic Ni/CNT catalyst upon introduction of Fe into the samples. As shown in Table 1, the Ni/Fe atomic ratios revealed by the XPS results are lower than those in the ICP-OES results demonstrating that Fe easily segregated on the particle surface. Similarly, previous study [46] indicated that the cohesive energy of Ni is slightly higher than that of Fe. In addition, the HS-LEIS results show that Ni coexisted with Fe on the outermost surface of Ni–Fe nanoparticles even if Fe would segregate on the surface (Figure S6). Therefore, it is presumable that the Fe^0 species interacted with Ni^0 by forming Ni–Fe alloys and were located on the Ni domain, whereas the iron oxides were doped on the Ni–Fe nanoparticles. Table S2 shows the Ni/C and Fe/C atomic surface ratios of Ni–Fe/CNT catalysts from XPS peak fitting. The Ni/C atomic surface ratio represents the relative Ni dispersion on the surface of CNT. Despite the smaller loading of Ni, the Ni/C atomic surface ratio of Ni_5–Fe_1/CNT is higher than that of monometallic Ni/CNT catalyst (0.040 and 0.021, respectively), which suggested that the introduction of Fe increased the Ni dispersion on the surface of support; these findings are consistent with the XRD and TEM results; similar results were observed in previous reports [46,47].

Figure 4 shows the H_2-TPR reduction profiles of the as-calcined catalyst precursors containing different Ni/Fe ratios under a total metal loading of 7 wt%. The monometallic Ni/CNT exhibited a distinct reduction peak at approximately 579 K with a shoulder peak at approximately 679 K. In previous reports [44,48,49], the reducibility of Ni species may be

affected by the nature of the support used and the synthesis conditions. Zhang [48] et al. investigated the reduction of Ni-deposited-CNTs and sample bulk NiO, suggesting that the reduction temperature of high-dispersed NiO nanoparticles is lower than bulk NiO. The first reduction peak of Ni/CNT at approximately 579 K is assigned to the reduction of high-dispersed NiO nanoparticles, and the shoulder peak assigned to the reduction of bigger NiO particles or some bulk NiO. The H_2-TPR reduction profile of Fe/CNT is different from those of the other samples. We observed that a tiny reduction peak appeared at approximately 667 K over Fe/CNT catalyst which is ascribed to the reduction of Fe_2O_3 to Fe_3O_4. However, the H_2 consumption is smaller than other catalysts which means only trace Fe^{3+} oxides were reduced. In addition, the reduction peak above 835 K is assigned to the reduction of iron oxides to Fe^0 species and the interaction of FeO with C species [42]. This result reveals that Fe species are more difficult to be reduced than the Ni species. The H_2 consumption peak of the as-calcined precursors containing different Ni/Fe ratios shifted to low temperatures with increasing Ni content. Compared with Fe/CNT, Ni_1–Fe_5/CNT showed a larger H_2 consumption peak, demonstrating that Ni promoted the reduction of Fe species. Furthermore, with decreasing Ni/Fe atomic ratios, the shoulder peak of Ni disappeared and formed a larger reduction peak which suggested that the introduction of Fe improved the Ni dispersion. It is reported that close interaction between metal species can promote or inhibit the reduction of metal oxides [47,50]. In our case, Ni and Fe species possibly formed Ni–Fe alloys and Ni efficiently dissociates H_2. In addition, H_2 consumption peak at 769 K decreased with decreasing Ni content; this finding is consistent with the H_2 consumption of amorphous C species and reduction in the C functional group in the presence of metals

[46,51].

The defect densities of the synthesized Ni–Fe/CNT catalysts were verified through analysis of the Raman spectra (Figure S7). Two peaks with a shoulder peak were observed at approximately 1340 and 1571 cm^{-1}, which are ascribed to the disordered graphite structure (D-band) and the ideal graphitic lattice vibration mode of Raman-active E_{2g} phonon of sp^2–C atoms (G-band), respectively. High I_D/I_G ratios, denoted as R, suggest the high extent of defects in CNTs. The I_D/I_G ratios for original and pretreated CNTs are 0.77 and 0.89; hence, the pretreated CNTs contained more defects than the original CNTs, whose surfaces can facilitate loading metal particles. With increasing Ni content, the R values of the supported samples ranged from 0.84 to 0.90, which are lower than those of the pretreated CNTs. These results indicate that the loaded metal particles occupied the defects on the surface of CNTs decreasing amount of defects. However, increase Fe loading slightly increased the number of defects.

To summarize, the results of XRD, TPR, and STEM analyses reveal the formation of Ni–Fe alloys assigned as Fe_1–Ni_3 structure which is ascribed to the interaction between Ni and Fe species. In situ XPS and HS-LEIS characterizations show that several species, such as Ni–Fe alloy and Fe oxides, presented on the surface of catalysts, and Fe species preferentially segregated on the surface of particles. In addition, these results show that the nanoparticle size decreased with decreasing Ni/Fe atomic ratio, which suggested that Fe promoted the dispersion of Ni.

3.2. HDO of guaiacol

Of all carbon materials tested, CNTs were found to be the optimal supports (Table S3) and the CNT-supported catalysts demonstrated excellent performance for HDO of guaiacol. The pristine CNTs showed a negligible activity of 0.5% conversion at 573 K, and the acid-treated CNTs displayed no activity. All CNTs required pretreatment to remove residual catalysts before using for the preparation Ni–Fe/CNT catalysts. In all cases, the main C1 products over the Ni–Fe/CNT catalysts are methane and methanol (Figure 5, above the columns). Catechol, the product of demethylation, was not detected by FID. The superior behavior is presumably due to the integrating properties of bimetals and CNTs for enhancing the absorption and activation of reactants. In this study, 2-methoxycyclohexanol was not detected, demonstrating that demethylation and demethoxylation occurred prior to the hydrogenation of aromatic rings. Additionally, trace products of transalkylation, such as cresol, and products of aromatic ring condensation, were detected by GC-MS analysis from the liquid products obtained through condensation. These products and some other unknown products are classified as "Others" in the tables.

3.2.1 HDO of guaiacol over Ni–Fe/CNT catalysts containing different Ni/Fe atomic ratios

Figure 5 shows the effect of Ni/Fe atomic ratio on the catalytic performance. Monometallic Ni/CNT demonstrated a high conversion activity of 79.0% but poor selectivity, meaning that the reaction pathways for the different products are energetically similar. The major products included cyclohexane and cyclohexanol, while phenol and "Others" like cresols were also observed over Ni/CNT catalyst. Previous reports indicated that Ni can efficiently dissociate H_2, which is used as active metal in hydrogenation of

aromatic rings [43,52]. Hence, hydrogenation of aromatic rings during guaiacol conversion easily occurred after demethylation and demethoxylation over the Ni/CNT catalysts. However, the Fe/CNT catalyst showed lower catalytic activity than Ni/CNT, and the major product of aromatic rings was phenol, in contrast to that of other Ni-based catalysts. Therefore, Fe species demonstrated poor performance in guaiacol hydrogenation. Similarly, Olcese et al. [26] reported that Fe/SiO_2 demonstrated deoxygenation activity without saturation of aromatic rings during conversion of guaiacol. However, the conversion of guaiacol and the selectivity of cyclohexane were promoted significantly upon introduction of a small amount of Fe into the catalysts studied. The selectivity of cyclohexane presented a volcano curve with decreasing Ni/Fe atomic ratio. The Ni_5–Fe_1/CNT catalyst showed higher selectivity of cyclohexane and conversion of 83.4% and 96.8%, respectively, compared with the other catalysts (Figure 5). This result indicated that the synergistic effect of bimetallic Ni–Fe catalysts promote the performance of HDO facilitating a reaction mechanism. The synergy between Ni and Fe is commonly observable, Sitthisa et al. [50] investigated the possible adsorption of furfural on the surface of Ni(111) and Ni–Fe(111) alloy through DFT calculations. The furan ring is preferentially adsorbed on the surface of the Fe domain because of its oxophilic nature. The strong interaction between Ni–Fe and furfural resulted in satisfactory conversion and selectivity. Sun et al. [30] studied the adsorption energies of phenol on the surface of Pd–Fe alloy through DFT calculations and revealed that Fe species favorably adsorbed phenol and weakened the C–O bond. Furthermore, the conversion and selectivity decreased with decreasing Ni/Fe atomic ratio. The conversion of guaiacol and the selectivity of cyclohexane over the Ni_2–Fe_1/CNT

catalyst are 85.0% and 78.7%, respectively. For the Ni_1–Fe_1/CNT catalyst in our case, the reaction showed a conversion of 75.0% and a cyclohexane selectivity of 39.1%. Apparently, addition of suitable Fe content enhanced the HDO of guaiacol. This phenomenon could be due to the fact that the HDO of guaiacol requires dissociation of H_2 on Ni species and adsorption of the O species of the substrate on Fe species to induce the cleavage of the C–O bond, corresponding to the TOF values summarized in Table 1. The amount of Ni species on the surface decreased with decreasing Ni/Fe atomic ratio (the total metal loading was maintained at 7%), thereby reducing the number of active sites for hydrogen activation. Hence, the activated hydrogen atoms were considered insufficient for hydrogenolysis of C–O bond and hydrogenation of aromatic rings. Other catalysts were also evaluated by maintaining the Ni loading constant at 7% but varying Fe content (Table S4). When Fe was introduced into the Ni/CNT, the conversion increased from 79.0% to 100.0% with incremental increase in Fe content. The selectivity of cyclohexane increased at large increments from 53.0% to 89.2%, supporting our explanation above.

To investigate whether the formation of Ni–Fe alloy resulted in high conversion and selectivity, we designed a control experiment by physical mixing of Ni/CNT and Fe/CNT (Ni/Fe = 5:1) for forming a contrastive catalyst (Figure 5-h). The conversion is 69.0%, which is lower than that of Ni_5–Fe_1/CNT and Ni_2–Fe_1/CNT; moreover, the product distribution differed between the samples. The main product is cyclohexanol, which demonstrates a selectivity of 55.9%. This result indicates that improvement in catalytic activity over Ni–Fe/CNT is mainly ascribed to the formation of Ni–Fe alloys, as proven by XRD, TEM, and other characterization techniques.

The conversion of guaiacol and the selectivity of phenol over the Ni_1–Fe_5/CNT increased compared with that of Fe/CNT. The Ni_1–Fe_5/CNT catalyst showed an incremental conversion of 47.2% and a phenol selectivity of 82.3%. The main product of the reaction over Fe-based catalysts is phenol, in contrast with that of the reaction over Ni-based catalysts with saturation of aromatic rings. Fe demonstrated strong affinity to O but weak ability to adsorb and activate H_2. Thus, the preferred reaction was the hydrogenolysis of the C_{aryl}–OCH_3 bond over the Fe-based catalysts as the thermodynamic profile in Figure 6 indicates. Addition of small quantity of Ni increased the conversion of guaiacol and the selectivity of phenol as shown by the lower intermediate energy in C_{aryl}–OCH_3 scission mechanism on the $Fe_3Ni(111)$ energy profile. Hence, activation of hydrogen on the Ni surface is a necessary step to hydrogenolyze C_{aryl}–OCH_3 bonds. When the amount of Ni is adequate, phenol as the intermediate would further react with activated hydrogen, thereby increasing the amount of cyclohexanol and cyclohexane with increasing guaiacol conversion. Suitable Ni contents obviously increased the yield of phenol.

Given that Ni_5–Fe_1/CNT and Ni_1–Fe_5/CNT exhibited high selectivity of cyclohexane and phenol, respectively, we investigated the effects of WLHSV. Figure 8-a shows the effect of WLHSV on the performance of the Ni_5–Fe_1/CNT catalyst. The conversion and selectivity of cyclohexane increased from 58.9% to 99.8% and from 49.0% to 99.9%, respectively, as the WLHSV decreased from 12 to 3. The amount of cyclohexanol, as the major by-product, decreased with decreasing WLHSV; hence, cyclohexane was formed from cyclohexanol through the hydrogenolysis of the C_{alkyl}–OH bond. This result indicates that cyclohexanol, as an intermediate, reacts easily with H_2 as increasing residence time on the active sites,

resulting in increased amount of cyclohexane. Ni_1–Fe_5/CNT performed lower activity than the Ni_5–Fe_1/CNT catalyst (Figure 8-b). At high WLHSV (10 h^{-1}), the conversion was calculated as 22.1% with 65% selectivity of phenol. The "Others" were mainly M-cresol and P-cresol, which were identified through GC-MS and FID detector. Over the Ni_1–Fe_5/CNT catalyst, with decreasing WLHSV, the conversion and selectivity to phenol increased from 22.1% to 62.7% and from 64.9% to 83.7%, respectively, whereas the selectivity of "Others" decreased obviously. These findings suggest that decreased WLHSV, which corresponded to increase in residence time on the surface of the catalysts, the guaiacol reacted with H_2 adequately to form ~~high selectivity of~~ phenol with high selectivity and decrease the selectivity of "Others". It is known that not only catalytic properties but chemical stability of monometallic active phase can be significantly promoted through adding second metal to form bimetallic nanoparticles. Figure 9-a–b showed the conversion and the selectivity over on Ni–Fe catalysts as a function of time. For monometallic Ni/CNT, the initial conversion is approximately 80% and displayed a rapid deactivation after 5 h. The decrease of selectivity of cyclohexane and cyclohexanol revealed the disappearance of HDO ability. Whereas, both bimetallic Ni_5–Fe_1/CNT and Ni_1–Fe_5/CNT showed promoted stabilities without noticeable deactivation; the selectivity to cyclohexane and phenol slightly fluctuated the initial selectivities. XRD patterns and TEM images of fresh and spent catalysts (Figures S8 and S9) revealed that bimetallic nanoparticles showed less sintering in contrast to that of monometallic Ni/CNT and formed thermodynamically stable alloy structure which is presumable that cohesive energy decrease with the incorporation of Fe in agreement with previous reports [42,53].

Briefly, the results demonstrated the good performance of bimetallic Ni–Fe/CNT catalysts on the HDO and hydrogenolysis of guaiacol. Variation in Ni/Fe atomic ratios remarkably changed the distribution of products, resulting in tunable selectivity to phenol and cyclohexane. When the major domain was Ni species, the main products of the hydrogenation of aromatic rings include cyclohexanol and cyclohexane. The yield of cyclohexane peaked over the Ni_5–Fe_1/CNT catalyst. The formation of Ni–Fe alloys also enhanced the selectivity of cyclohexane. In addition, the reaction over the Fe-based catalysts produced phenol as the major product, and the selectivity of phenol peaked at the Ni/Fe atomic ratio of 0.2.

3.2.3 Effect of Ni-Fe nanoparticle size supported on CNT

To further investigate the effect of nanoparticle size for HDO of guaiacol over the Ni–Fe/CNT catalysts, we tuned the size of nanoparticles by using different reduction temperatures and evaluated monometallic Ni/CNT and Fe/CNT catalysts as well as the bimetallic Ni–Fe catalysts(Table 2). It is clear that both the size of the nanoparticles and the chemical state of nanoparticles changed obviously by using different reduction temperature. In order to exclude the interference of changes of chemical state, we carried out the XPS characterizations of Ni_5–Fe_1/CNT catalysts reduced at 673 K, 773 K, and 873 K, respectively. Ni and Fe concentrations were calculated by peak fitting (Figure S10) and summarized in Table S5. We observed that Ni^0 concentration had a slight increase from 38.0% to 44.3% while Fe^0 concentration increase greatly from 9.1% to 26% with the increase of reduction temperature. However, the catalytic performances decreased even the extent of

reduction increased; so we suggested the effect of nanoparticles size is the main factor that influences the catalytic performance than changes of nature of nanoparticles on the surface. (rather than changed in the nature of nanoparticles on the surface?).

Nanoparticle size increased with increasing reduction temperature over the Ni/CNT catalysts. Entries 1–3 show the performance for HDO of guaiacol over Ni/CNT, which was reduced at 673, 773, and 873 K, respectively. The selectivity of cyclohexane decreased sharply from 53.0% to 4.6%, and the selectivity of cyclohexanol increased from 31.7% to 69.7% with increasing nanoparticle size; however, the conversion slightly fluctuated within 77%–81%. Moreover, phenol over Entry 3 rapidly increased and reached a selectivity of 10.4%. This phenomenon reveals that reaction activity decreased with increasing nanoparticle size, resulting in reduced ability for hydrogenation of aromatic rings and hydrogenolysis of C_{alkyl}–OH bonds. These results are consistent with those of previous studies, which showed that small metal particles are beneficial for hydrogenation reactions, whereas large particles and bulks can weakly activate hydrogen [54,55]. The tendency of activities over Ni_5–Fe_1/CNT catalysts from Entries 4–6 is similar to that over monometallic Ni/CNT catalysts. Cyclohexane rapidly decreased and cyclohexanol increased with increasing nanoparticle size. A slight discrepancy was observed, that is, no phenol was produced in the reactions over the three Ni_5–Fe_1/CNT catalysts. Furthermore, comparison of activity between Ni/CNT and Ni_5–Fe_1/CNT indicated that the bimetallic Ni_5–Fe_1/CNT catalysts always displayed improved performance than Ni/CNT catalysts at the same reduction temperature. This finding reveals that addition of Fe species enable improved dispersion of nanoparticle and promote hydrogenolysis of C_{alkyl}–OH bonds. Compared with

that of Ni-based catalysts, the nanoparticle size of Fe-based catalysts showed less sensitivity to reduction temperature. Entries 7–9 exhibited similar particle sizes, despite that they were reduced at 673, 773, and 873 K, respectively; this finding corresponds to similar activity over the three catalysts. The main product is phenol, and the conversion and selectivity are approximately 40%–50% and 80%, respectively. The by-product cyclohexanol was also observed, indicating that a competitive relationship existed between cleavage of C_{aryl}–OCH_3 bond and hydrogenation of phenol. For the Fe/CNT catalysts, Entry 11 showed improved performance than Entry 10, despite their similar nanoparticle sizes; hence, Fe^0 species was beneficial for hydrogenolysis of guaiacol. The catalyst of Entry 12 with a size of 11.5 nm displayed weak activity. Thus, a small metallic particle is preferred for cleavage of C–O bonds and HDO of guaiacol.

To better understand the essence of effect of nanoparticle size on catalytic behaviour, the TOF values were also calculated and summarized in Table 2. Ni/CNT catalysts with different nanoparticle size (Entry 1–3) exhibited similar TOF values but quite different product distributions, indicating that in addition to the simple relationship between the amount of surface metal atoms and the catalytic activity, some complicated correlations on the formation of catalytic sites with hydrogenation of aromatic ring and hydrogenolysis of C-O bond also existed. The different distributions of products suggested that the conversion of guaiacol is a structure-sensitive reaction. Mortensen [56] et al. observed a strong influence of nickel particle size on HDO of phenol and suggested that the large particles are very active for hydrogenation of aromatic ring while small particles are required to facilitate deoxygenation; it is consistent with our results. Ni_5–Fe_1/CNT catalysts displayed similar

trend with Ni/CNT but performed higher TOF values and better selectivity of deoxygenation products, which is ascribed to modification of Fe to the surface of nanoparticles. To summarize, the effect of nanoparticles caused by different reduction temperature and Fe modification to the surface of nanoparticles truly influenced the catalytic activity and selectivity.

3.2.3 HDO network of guaiacol over Ni–Fe/CNT catalysts

Several reaction networks for HDO of guaiacol have been proposed to elucidate the reaction pathways over different catalysts [2,6,13]. Demethylation and demethoxylation was proposed to be the first step in reaction pathways . In many cases, methane is the by-product of demethylation over various catalysts, such as Ru/MgO, Ru/C, and Fe/SiO_2 [11,19,26]. Previous studies reported that demethylation occurred on activated metal sites, and methyl group remained on the surface [6,57]. As an alternative pathway, methanol and phenol are formed through the cleavage of C_{aryl}–OCH_3, which explains the presence of CH_3OH. The demethoxylation reaction was observed over several catalysts, such as sulfided Co–Mo/Al_2O_3, Co–Mo/ZrO_2, and supported Ni_2P. Phenol can be deoxygenated to obtain completely deoxygenated products. However, the conversion of phenol proceeded in different pathways, depending on the activated species of catalysts. Studies showed that the hydrogenation of the aromatic ring occur before dehydroxylation of phenol over many catalysts [6,13,58]. Moreover, transalkylation occurs during HDO of guaiacol, especially on Lewis acidic catalysts [21,22]. Consequently, different products (i.e., phenol, benzene, cyclohexanol, cyclohexane, and catechol) can be obtained by controlling the reaction

pathways over different catalysts.

Scheme 1 illustrates the proposed pathways of CNT-supported Ni–Fe bimetallic catalyst used in this study. Methane and methanol were observed as C1 by-products during the HDO of guaiacol over Ni–Fe bimetallic catalysts, indicating that both demethylation and demethoxylation occurred in the reaction. However, no catechol was detected in all cases, suggesting that this compound was rapidly deoxygenated into phenol. In addition, we introduced pure methanol to the reactor as a blank test and observed the production of methane. That is to say, methane can also be derived from the CH_3OH reduction. Phenol is the major intermediate formed from demethoxylation of guaiacol. Phenol can further react to yield products with saturated rings in some catalysts, such as Ni/CNT and Ni_5–Fe_1/CNT. Consistent with data presented in Figure 5, trace benzene was observed, and products with saturated rings (cyclohexanol and cyclohexane) were found to be the major products. Furthermore, cyclohexene and the products of aromatic rings were observed by analyzing the mixture collected through condensation by using GC-MS (Figure S11). Table S6 also shows the conversion of phenol as the intermediate compound at which case that cyclohexanon and cyclohexanol could be observed. These results suggest that phenol hydrogenation occurred before the cleavage of the last HO–Ar. Cyclohexanol can be further deoxygenated when suitable Fe contents were introduced.

To elucidate the synergism of Ni–Fe nanoparticles for HDO of guaiacol over Ni–Fe bimetallic catalysts containing various Ni/Fe atomic ratios, we propose appropriate reaction mechanisms in Scheme 2. Our results showed that saturation of aromatic rings over monometallic Ni/CNT catalyst is favored to produce cyclohexanol and cyclohexane. As

depicted in Scheme 2-a, Ni demonstrated high hydrogen absorption and activation abilities but weak substrate absorption. After demethoxylation of guaiacol, phenol can be adsorbed plainly on the Ni surface and then react with activated hydrogen to form cyclohexanol. However, cyclohexanol can hardly further react to yield cyclohexane because of weak oxygen affinity, causing low selectivity of cyclohexane. When suitable Fe contents were introduced into the surface of Ni, the HDO ability of catalyst was considerably enhanced, as shown in Scheme 2-b. Compared with Ni species, Fe demonstrated strong activation of the molecule, though the binding is weaker by 48.24 kJ/mol. On the surface of Ni–Fe nanoparticles, Fe sites stabilizes intermediates, while Ni sites favors the adsorption of activated hydrogen. This behavior was also observed in Pd–Fe catalysts, in which Fe is likely the active site for HDO of phenol. Figure 5 shows that the selectivity of cyclohexanol and phenol increased when the Ni/Fe atomic ratios are < 2. This phenomenon reveals that further hydrogenation and hydrogenolysis of the C_{alkyl}–OH bond require a sufficient amount of activated hydrogen on the surface of Ni, as proven by the result of additional experiments (Table 3). Scheme 2-c shows a proper reaction pathway on the surface of the Fe/CNT catalyst. Some activated substrates reacted with hydrogen to yield phenol, whereas other substrates occurred by-reaction such as oligomerization to form by-products unrecognized in the absence of sufficient amounts of activated hydrogen. In the case of Ni_1–Fe_5/CNT as described in Scheme 2-d, when a small amount of Ni was introduced into Fe surface, the dissociation of H_2 greatly enhanced, thereby increasing the selectivity of phenol.

The enhanced effect for HDO of guaiacol could be due to the synergism between Ni and Fe species. Ni promoted dissociation of H_2, whereas Fe played a crucial role in oxygen

affinity. Different amounts of Ni and Fe in the catalysts remarkably changed the distribution of products. High selectivity of cyclohexane and phenol can be obtained by controlling the content of Ni and Fe, an approach that is easy to operate.

Conclusions

In summary, non-precious Ni-Fe/CNT catalysts were investigated for efficient HDO of guaiacol. Product distribution can be tuned by changing the Ni/Fe atomic ratios, which can obtain 99.8% selectivity of cyclohexane and 83.7% selectivity of phenol under suitable conditions at Ni/Fe ratios of 5:1 and 1:5, respectively. A proper reaction mechanism was proposed to explain the results over Ni–Fe bimetallic catalysts. The enhanced effect is attributed to the interaction of Ni and Fe, and the formation of Ni–Fe alloy was observed by using TPR, XRD, and STEM analyses. The Fe and Ni species on the surface of Ni–Fe particles, which demonstrate strong π-system activation, i.e. aromatic ring, and high ability to dissociate H_2, exerted synergistic effect to enhance HDO of guaiacol. In addition, the investigation of effect of nanoparticle size over monometallic Ni/CNT and Fe/CNT catalysts as well as bimetallic Ni–Fe/CNT catalysts suggested that the conversion of guaiacol is a structure-sensitive reaction, which influenced the catalytic activity and selectivity greatly.

.

Acknowledgements

We acknowledge the financial support from the Natural Science Foundation of China

(21303141, 21403178, 21473145 and 91545115), and the Program for Innovative Research Team in Chinese Universities (No. IRT_14R31). The authors also acknowledge the use of the Advanced Research Computing @ Cardiff (ARCCA) at Cardiff University, and associated support services.

References

[1] A. J. Ragauskas, C. K. Williams, B. H. Davison, G. Britovsek, J. Cairney, C. A. Eckert, W. J. Frederick Jr., J. P. Hallett, D. J. Leak, C. L. Liotta, J. R. Mielenz, R. Murphy, R. Templer, T. Tschaplinski, Science, 311 (2006) 484–489.

[2] J. Zakzeski, P. C. A. Bruijnincx, A. L. Jongerius, B. M. Weckhuysen, Chem. Rev., 110 (2010) 3552–3599.

[3] G. W. Huber, S. Iborra, A. Corma, Chem. Rev., 106 (2006) 4044–4098.

[4] C. Li, X. Zhao, A. Wang, G. W. Huber, T. Zhang, Chem. Rev., 115 (2015) 11559–11624.

[5] J. C. Serrano-Ruiz, J. A. Dumesic, Energ. Environ. Sci., 4 (2011) 83–99.

[6] M. Saidi, F. Samimi, D. Karimipourfard, T. Nimmanwudipong, B. C. Gates, M. R. Rahimpour, Energ. Environ. Sci., 7 (2014) 103–129.

[7] J. E. Holladay, J. J. Bozell, J. F. White, D. Johnson, Report PNNL, (2007).

[8] R. Rinaldi, F. Schüth, Energ. Environ. Sci., 2 (2009) 610–626.

[9] I. Graça, J. M. Lopes, M. F. Ribeiro, F. Ramôa Ribeiro, H. S. Cerqueira, M. B. B. de Almeida, Appl. Catal. B-Environ., 101 (2011) 613–621.

[10] P. R. Patwardhan, R. C. Brown, B. H. Shanks, ChemSusChem, 4 (2011) 1629–1636.

[11] Y. Nakagawa, M. Ishikawa, M. Tamura, K. Tomishige, Green Chem., 16 (2014) 2197–2203.

[12] S. K. Wu, P. C. Lai, Y. C. Lin, H. P. Wan, H. T. Lee, Y. H. Chang, ACS Sustain. Chem. Eng., 1 (2013) 349–358.

[13] Y. K. Hong, D. W. Lee, H. J. Eom, K. Y. Lee, Appl. Catal. B-Environ., 150–151 (2014) 438–445.

[14] A. Centeno, E. Laurent, B. Delmon, J. Catal., 154 (1995) 288–298.

[15] A. L. Jongerius, R. Jastrzebski, P. C. A. Bruijnincx, B. M. Weckhuysen, J. Catal., 285 (2012) 315–323.

[16] M. Badawi, J. F. Paul, S. Cristol, E. Payen, Y. Romero, F. Richard, S. Brunet, D. Lambert, X. Portier, A. Popov, E. Kondratieva, J. M. Goupil, J. El Fallah, J. P. Gilson, L. Mariey, A. Travert, F. Maugé, J. Catal., 282 (2011) 155–164.

[17] X. L. Ma, K. Sakanishi, I. Mochida, Ind. Eng. Chem. Res., 33 (1994) 218–222.

[18] O. İ. Şenol, T. R. Viljava, A. O. I. Krause, Appl. Catal. A-Gen., 326 (2007) 236–244.

[19] A. Sanna, T. P. Vispute, G. W. Huber, Appl. Catal. B-Environ., 165 (2015) 446–456.

[20] X. Zhu, L. L. Lobban, R. G. Mallinson, D. E. Resasco, J. Catal., 281 (2011) 21–29.

[21] T. Nimmanwudipong, C. Aydin, J. Lu, R. C. Runnebaum, K. C. Brodwater, N. D. Browning, D. E. Block, B. C. Gates, Catal. Lett., 142 (2012) 1190–1196.

[22] T. Nimmanwudipong, R. C. Runnebaum, D. E. Block, B. C. Gates, Energ. Fuel, 25 (2011) 3417–3427.

[23] D. Gao, C. Schweitzer, H. T. Hwang, A. Varma, Ind. Eng. Chem. Res., 53 (2014) 18658–18667.

[24] X. Zhang, T. Wang, L. Ma, Q. Zhang, Y. Yu, Q. Liu, Catal. Commun., 33 (2013) 15–19.

[25] R. Olcese, M. M. Bettahar, B. Malaman, J. Ghanbaja, L. Tibavizco, D. Petitjean, A. Dufour, Appl. Catal. B-Environ., 129 (2013) 528–538.

[26] R. N. Olcese, M. Bettahar, D. Petitjean, B. Malaman, F. Giovanella, A. Dufour, Appl. Catal. B-Environ., 115-116 (2012) 63–73.

[27] W. Song, Y. Liu, E. Baráth, C. Zhao, J. A. Lercher, Green Chem., 17 (2015) 1204–1218.

[28] A. R. Ardiyanti, S. A. Khromova, R. H. Venderbosch, V. A. Yakovlev, H. J. Heeres, Appl. Catal. B-Environ., 117–118 (2012) 105–117.

[29] A. B. Dongil, L. Pastor-Pérez, A. Sepúlveda-Escribano, R. García, N. Escalona, Fuel, 172 (2016) 65–69.

[30] J. Sun, A. M. Karim, H. Zhang, L. Kovarik, X. S. Li, A. J. Hensley, J. S. McEwen, Y. Wang, J. Catal., 306 (2013) 47–57.

[31] P. Luksirikul, K. Tedsree, M. G. Moloney, M. L. Green, S. C. Tsang, Angew. Chem. Int. Ed., 51 (2012) 6998–7001.

[32] P. Zhang, C. L. Shao, Z. Y. Zhang. M. Y. Zhang, J. B. Mu, Z. C. Guo, Y. C. Liu. Nanoscale 3 (2011) 3357–3363.

[33] G. Kresse, J. Hafner, Phys. Rev. B, 47 (1993) 558–561.

[34] G. Kresse, J. Furthmüller, Comput. Mat. Sci., 6 (1996) 15–50.

[35] N. D.Mermin, Phys. Rev., 137 (1965) 1441–1443.

[36] J. Perdew, A. Ruzsinszky, G. Csonka, O. Vydrov, G. Scuseria, L. Constantin, X. Zhou, K.Burke, Phys. Rev. Lett., 100 (2008) 136406.

[37] S. Grimme, J. Comput. Chem., 27 (2006) 1787–1799.

[38] S. Irrera, A. Roldan, G. Portalone, N. H. de Leeuw, J. Phys. Chem. C, 117 (2013) 3949–3957.

[39] S. S. Tafreshi, A. Roldan, N. Y. Dzade, N. H. de Leeuw, Surf. Sci., 622 (2014) 1–8.

[40] N. Dzade,; A. Roldan, N. H. de Leeuw, Minerals, 4 (2014) 89–115.

[41] H. J. Monkhorst, J. D. Pack, Phys. Rev. B, 13 (1976) 5188–5192.

[42] X. Yu, J. Chen, T. Ren, RSC Adv., 4 (2014) 46427–46436.

[43] L. Nie, P. M. de Souza, F. B. Noronha, W. An, T. Sooknoi, D. E. Resasco, J. Mol. Catal. A-chem., 388–389 (2014) 47–55.

[44] A. B. Dongil, I. T. Ghampson, R. Garc´ıa, J. L. G. Fierro, N. Escalona. RSC Adv., 6 (2016) 2611–2623

[45] A. B. Dongil, B. Bachiller-Baeza, I. Rodr´ıguez-Ramos, J. L. G. Fierro, N. Escalona. RSC Adv., 6 (2016) 26658–26667

[46] B. Li, J. Wang, Y. Yuan, H. Ariga, S. Takakusagi, K. Asakura, ACS Catal., 1 (2011) 1521–1528.

[47] S. Leng, X. Wang, X. He, L. Liu, Y. E. Liu, X. Zhong, G. Zhuang, J. G. Wang, Catal. Commun., 41 (2013) 34–37.

[48] H. X. Yang, S. Q. Song, R. C. Rao, X. Z. Wang, Q. Yu, A. M. Zhang. J. Mol. Catal. A-chem., 1–2 (2010) 33–39.

[49] S. H. Lu, C. Zhang, Y. Liu. Int. J. Hydreogen Energ., 3 (2011) 1939–1948.

[50] S. Sitthisa, W. An, D. E. Resasco, J. Catal., 284 (2011) 90–101.

[51] A. Nieto-Márquez, S. Gil, A. Romero, J. L. Valverde, S. Gómez-Quero, M. A. Keane,

Appl. Catal. A-Gen., 363 (2009) 188–198.

[52] H. Shafaghat, P. S. Rezaei, W. M. A. W. Daud. J. Ind. Eng. Chem., 35 (2016) 268–176.

[53] Y. Mishin, M. J. Mehl, D. A. Papaconstantopoulos. Acta Mater., 53 (2005) 4029–4041.

[54] J. H. Kima, D. J. Suh,T. J. Parkb, K. L. Kima, Appl. Catal. A-Gen., 197 (2000) 191–200.

[55] M. Ojeda, S. Rojas, M. Boutonnet, F. J. Pérez-Alonso, F. Javier García-García, J. L. G. Fierro, Appl. Catal. A-Gen., 274 (2004) 33–41.

[56] P. M. Mortensen, J. D. Grunwaldt, P. A. Jensen, A. D. Jensen. Catal. Today, 259 (2016) 277–284.

[57] L. Souza Macedo, D. R. Stellwagen, V. Teixeira da Silva, J. H. Bitter, ChemCatChem, 7 (2015) 2816–2823.

[58] Q. Tan, G. Wang, L. Nie, A. Dinse, C. Buda, J. Shabaker, D. E. Resasco, ACS Catal., 5 (2015) 6271–6283.

Table/Figure Captions

Table 1 Physicochemical properties and catalytic performance of Ni–Fe/CNT catalysts

Table 2 Catalytic performance of monometallic Ni/CNT and Fe/CNT catalysts and the bimetallic Ni–Fe catalysts under different reduction temperatures

Scheme 1 Reaction pathways for HDO of guaiacol on Ni–Fe/CNT bimetallic catalysts.

Scheme 2 Appropriate reaction mechanisms for HDO of guaiacol. (a) Ni/CNT, (b) Ni_5–Fe_1/CNT, (c) Fe/CNT, and (d) Ni_1–Fe_5/CNT.

Figure 1 XRD patterns of Ni–Fe/CNT catalysts reduced at 673 K under different Ni/Fe atomic ratios: (a) CNT, (b) Ni/CNT, (c) Ni_5–Fe_1/CNT, (d) Ni_2–Fe_1/CNT, (e) Ni_1–Fe_1/CNT, (f) Ni_1–Fe_2/CNT, (g) Ni_1–Fe_5/CNT, and (h) Fe/CNT.

Figure 2 (A) HRTEM image, **(B)** STEM-EDX mapping and **(C)** linear scanning of as-reduced Ni_5–Fe_1/CNT catalyst.

Figure 3 (A) Fe 2p XPS spectra: (a) Fe/CNT, (b) Ni_2–Fe_1/CNT, and (c) Ni_5–Fe_1/CNT; **(B)** Ni 2p XPS spectra: (a) Ni/CNT, (b) Ni_2–Fe_1/CNT, and (c) Ni_5–Fe_1/CNT.

Figure 4 H_2-TPR profiles of Ni–Fe/CNT catalysts containing different Ni/Fe atomic ratios: (a) Ni/CNT, (b) Ni_5–Fe_1/CNT, (c) Ni_2–Fe_1/CNT, (d) Ni_1–Fe_1/CNT, (e) Ni_1–Fe_2/CNT, (f) Ni_1–Fe_5/CNT, and (g) Fe/CNT.

Figure 5 Catalytic performances of Ni–Fe/CNT catalysts containing different Ni/Fe atomic ratios. (a) Ni/CNT, (b) Ni_5–Fe_1/CNT, (c) Ni_2–Fe_1/CNT, (d) Ni_1–Fe_1/CNT, (e) Ni_1–Fe_2/CNT, (f) Ni_1–Fe_5/CNT, (g) Fe/CNT, and (h) Ni/CNT + Fe/CNT. Reaction conditions were as follows: $WLHSV_{GUA}$= 6.0 h^{-1}, P(H_2) = 3.0 MPa, H_2/GUA molar ratio = 50, T = 573 K.

Figure 6 Thermodynamic energy profile for guaiacol reduction on **(A)** pristine Ni(111) and **(B)** Fe_3Ni(111) surfaces. Each state corresponds to a single hydrogenation step leading to CH_3OH + Ph-OH (black line and representation insets) and H_2O + Ph-OCH_3 (blue line). Color scheme: light-grey represents Ni, grey is Fe, dark grey is C, red is O white is H and the co-adsorbed H is represented in blue.

Figure 7 Catalytic performances of catalysts with different WLHSV, P(H_2)=3.0 MPa, H_2/GUA molar ratio = 50, T= 573 K, (a) Ni_5Fe_1/CNT, (b) Ni_1Fe_5/CNT.

Figure 8 Conversion (a) and selectivity (b) on Ni/CNT, Ni_5–Fe_1/CNT, Ni_1–Fe_5/CNT catalysts as a function of time. Reaction conditions: $WLHSV_{GUA}$= 6.0 h^{-1}, P(H_2) = 3.0 MPa, H_2/GUA molar ratio = 50, T = 573 K.

Table 1 Physicochemical properties and catalytic performance of Ni–Fe/CNT catalysts

Sample	Total M loading[a] / wt. %	Ni/Fe atomic ratio		S_{BET} / m^2g^{-1}	D_{pore} / nm	CO uptake / μmol g^{-1}	Average particle size /nm		R[c] Valve	TOF[d] / h^{-1}
		By ICP	By XPS				By XRD[b]	By TEM		
CNT-O	–	–	–	147	24.1	–	–	–	0.89	–
Ni/CNT	7.07	∞	∞	145	15.3	72.4	9.2	8.7	0.84	275.9
Ni_5–Fe_1/CNT	6.59	4.41:1	1.69:1	145	14.8	67.5	7.7	7.3	0.85	370.2
Ni_2–Fe_1/CNT	6.02	2.08:1	0.59:1	149	15.8	37.6	7.0	6.9	0.85	276.4
Ni_1–Fe_1/CNT	5.93	1.06:1	–	153	15.2	21.3	6.3	6.2	0.87	222.4
Ni_1–Fe_2/CNT	6.38	0.46:1	–	159	13.4	14.3	5.9	5.7	0.89	170.7
Ni_1–Fe_5/CNT	5.49	0.27:1	–	150	17.5	13.7	5.3	5.3	0.89	104.5
Fe/CNT	6.42	0	0	138	23.0	11.6	6.0	5.1	0.90	41.1

[a] Metal loading determined by ICP-OES.

[b] Calculated by the Scherrer equation.

[c] R Value means I_D/I_G ratios calculated by Raman spectra.

[d] Calculated by metal dispersion.

Table 2 Catalytic performance of Ni/CNT, Fe/CNT and bimetallic Ni–Fe catalysts with different reduction temperature

Catalyst	Entry	RT / K	Particle size / nm	Conv. / %	Selectivity / %					C1 product selectivity / %		TOF / h^{-1}
							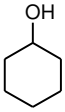	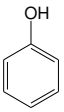	Others	CH_4	MeOH	
Ni/CNT	1	673	9.2	79.0	53.0	0.3	31.7	4.4	10.6	82.2%	9.3%	275.9
	2	773	13.5	80.2	24.7	0.7	58.3	1.0	15.3	58.9%	30.4%	262.3
	3	873	16.0	77.0	4.6	1.1	69.7	10.4	14.2	33.0%	50.9%	258.9
Ni_5–Fe_1 /CNT	4	673	7.7	96.8	83.4	3.2	12.7	0.0	0.7	85.4%	14.6%	370.2
	5	773	8.3	96.7	67.5	6.0	23.0	0.0	3.5	76.0%	22.0%	350.6
	6	873	11.2	99.0	55.8	4.2	31.9	0.0	8.1	61.7%	38.3%	342.5
Ni_1–Fe_5 /CNT	7	673	5.3	47.2	2.5	0.9	10.4	83.3	2.9	67.6%	24.5%	104.5
	8	773	5.7	41.3	2.4	0.8	13.2	79.4	4.2	40.7%	14.9%	98.7
	9	873	5.2	41.5	2.5	0.6	12.5	81.0	3.4	38.9%	13.8%	96.4
Fe/CNT	10	673	6.0	17.2	0.4	0.5	0.7	40.4	58.0	64.9%	24.3%	41.1
	11	773	6.0	19.3	0.0	0.0	1.6	92.9	5.5	57.5%	19.6%	45.8
	12	873	11.5	8.4	1.5	0.8	2.6	90.8	4.4	44.5%	5.6%	30.4

$WLHSV_{GUA}$= 6.0 h^{-1}, $P(H_2)$=3.0 MPa, H_2/GUA molar ratio = 50, T = 573 K; RT: Reduction temperature; TOF was calculated by metal dispersion at low conversion.

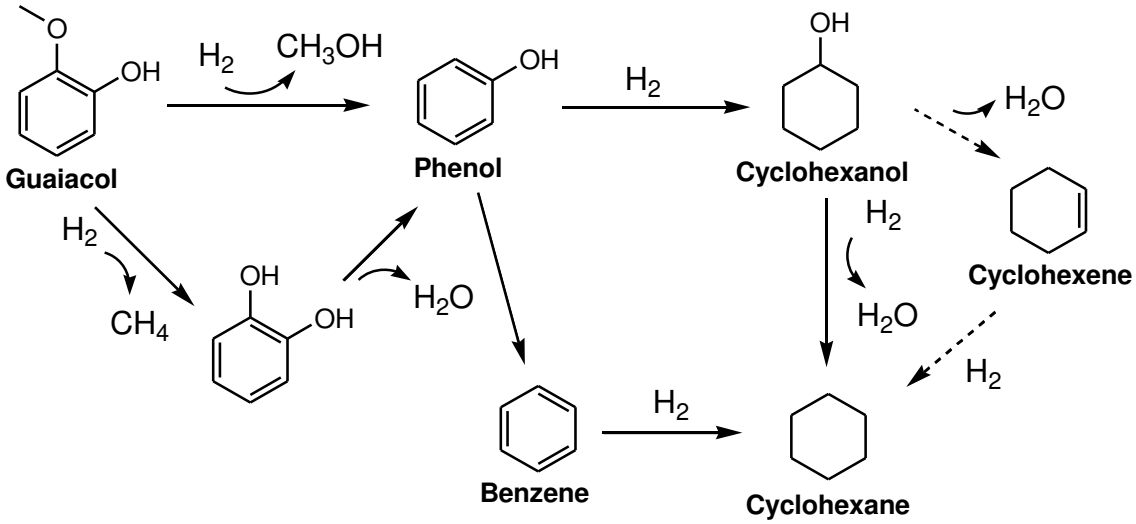

Scheme 1 Reaction pathways for HDO of guaiacol on Ni–Fe/CNT bimetallic catalysts.

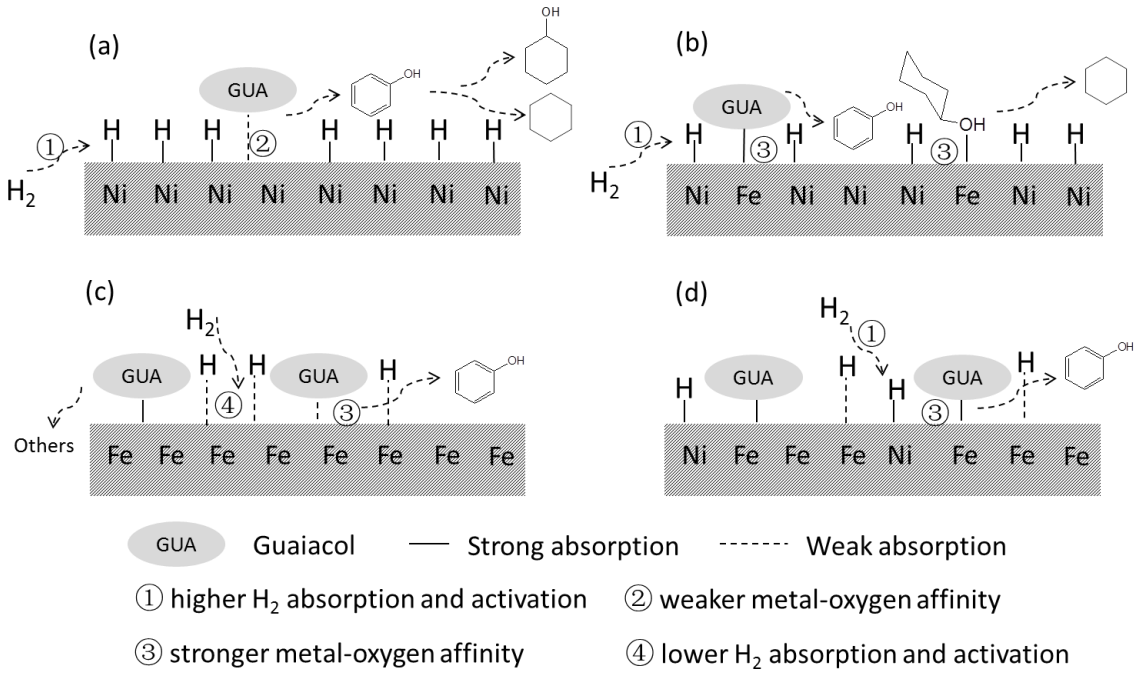

Scheme 2 Proper reaction mechanisms for HDO of guaiacol. (a) Ni/CNT, (b) Ni_5–Fe_1/CNT, (c) Fe/CNT, (d) Ni_1–Fe_5/CNT.

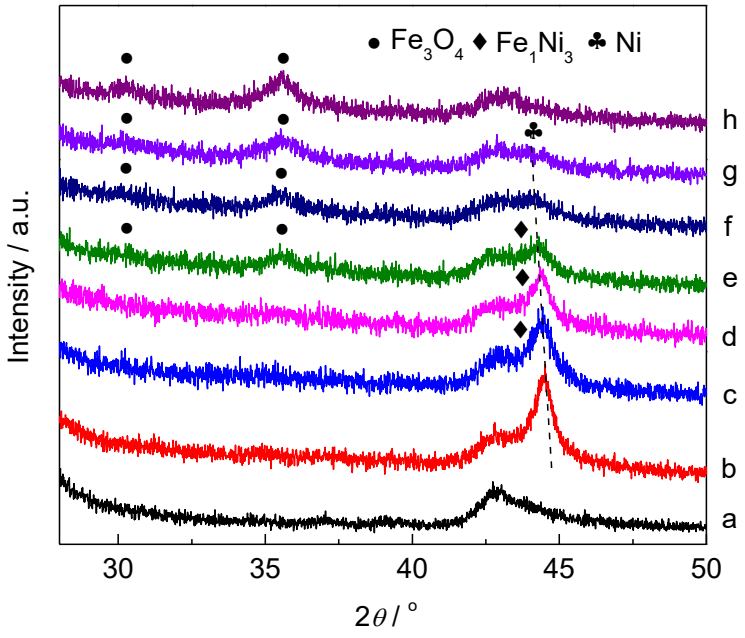

Figure 1 XRD patterns of Ni–Fe/CNT catalysts reduced at 673 K with different Ni/Fe atomic ratios: (a) CNT, (b) Ni/CNT, (c) Ni_5–Fe_1/CNT, (d) Ni_2–Fe_1/CNT, (e) Ni_1–Fe_1/CNT, (f) Ni_1–Fe_2/CNT, (g) Ni_1–Fe_5/CNT, (h) Fe/CNT.

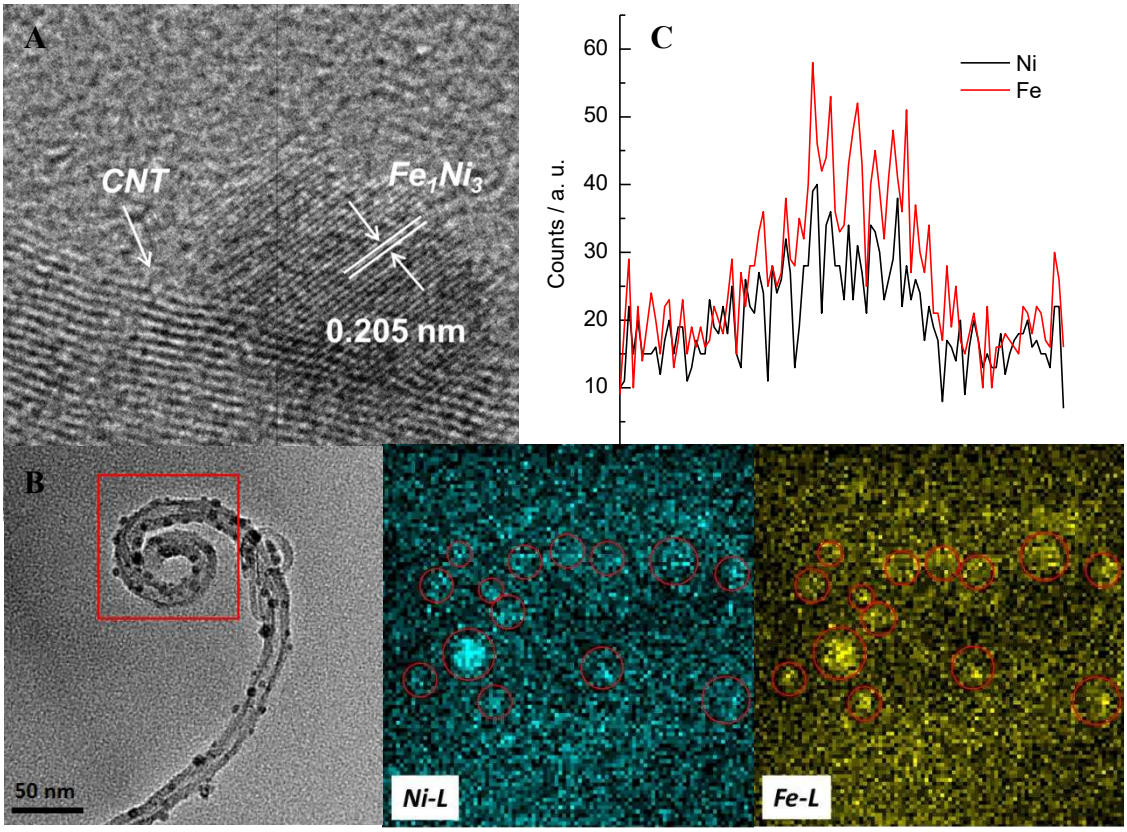

Figure 2 (A) HRTEM image, **(B)** STEM-EDX mapping and **(C)** linear scanning of as-reduced Ni_5–Fe_1/CNT catalyst.

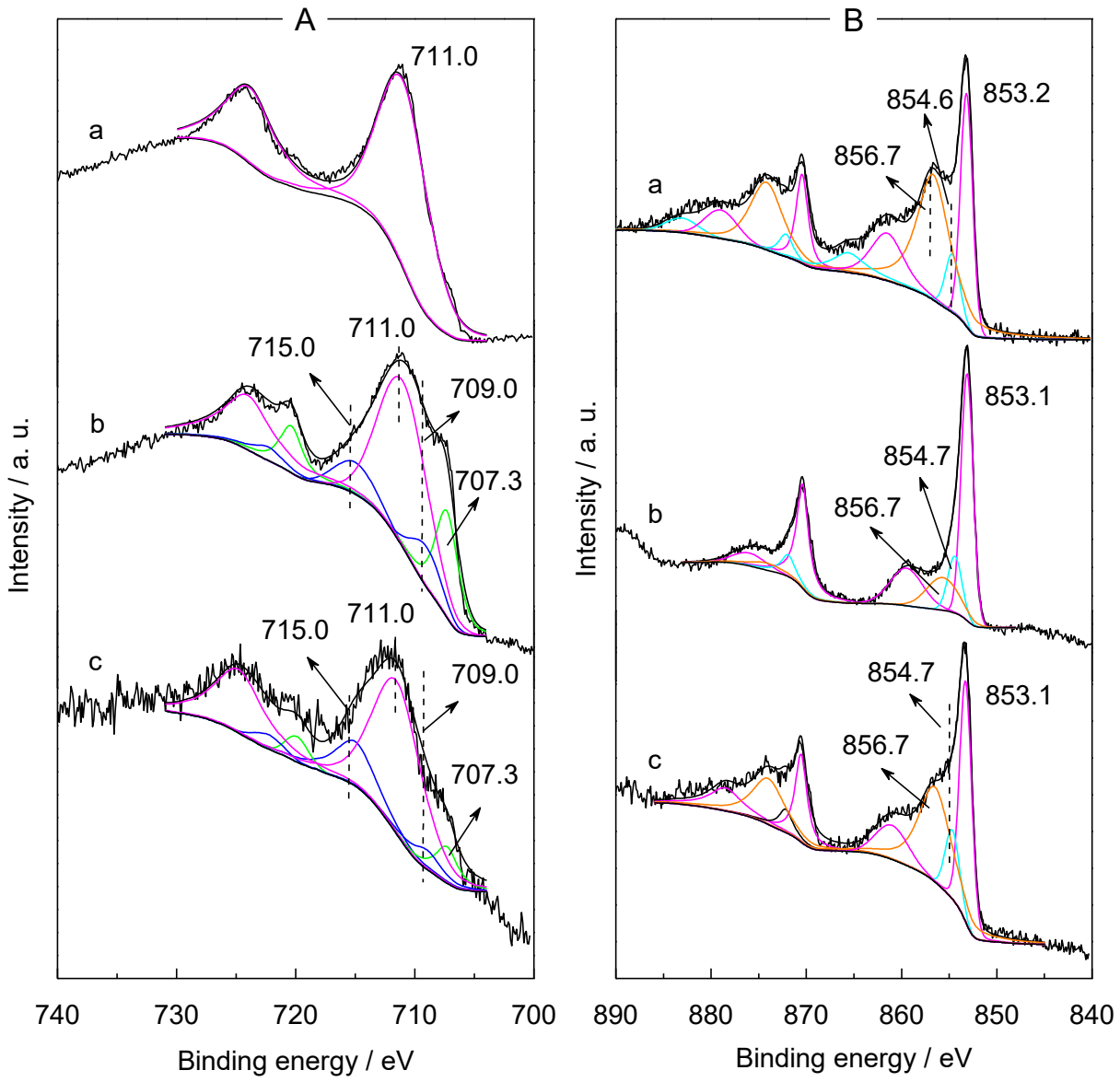

Figure 3 (A) Fe 2p XPS spectra: (a) Fe/CNT, (b) Ni_2–Fe_1/CNT, (c) Ni_5–Fe_1/CNT; **(B)** Ni 2p XPS spectra: (a) Ni/CNT, (b) Ni_2–Fe_1/CNT, (c) Ni_5–Fe_1/CNT.

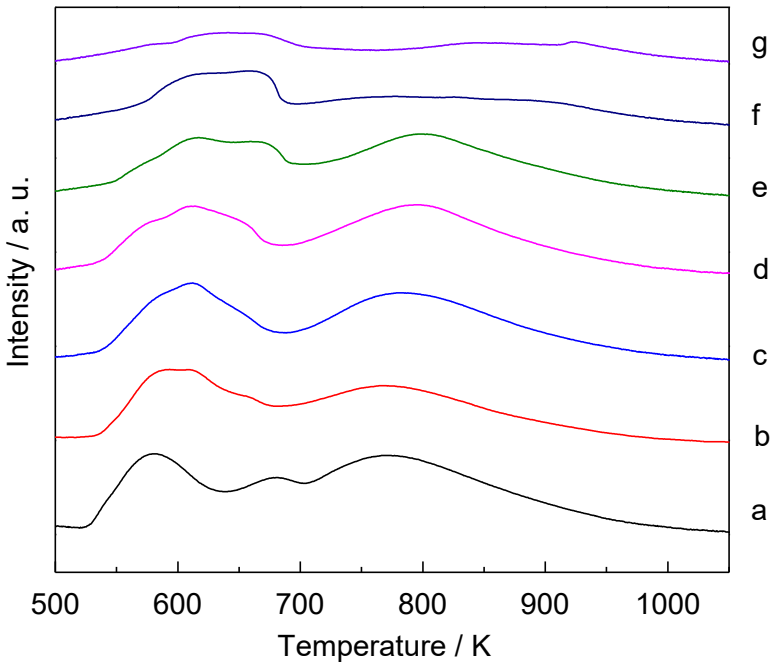

Figure 4 H_2-TPR profiles of Ni–Fe/CNT catalysts with different Ni/Fe atomic ratio: (a) Ni/CNT, (b) Ni_5–Fe_1/CNT, (c) Ni_2–Fe_1/CNT, (d) Ni_1–Fe_1/CNT, (e) Ni_1–Fe_2/CNT, (f) Ni_1–Fe_5/CNT, (g) Fe/CNT.

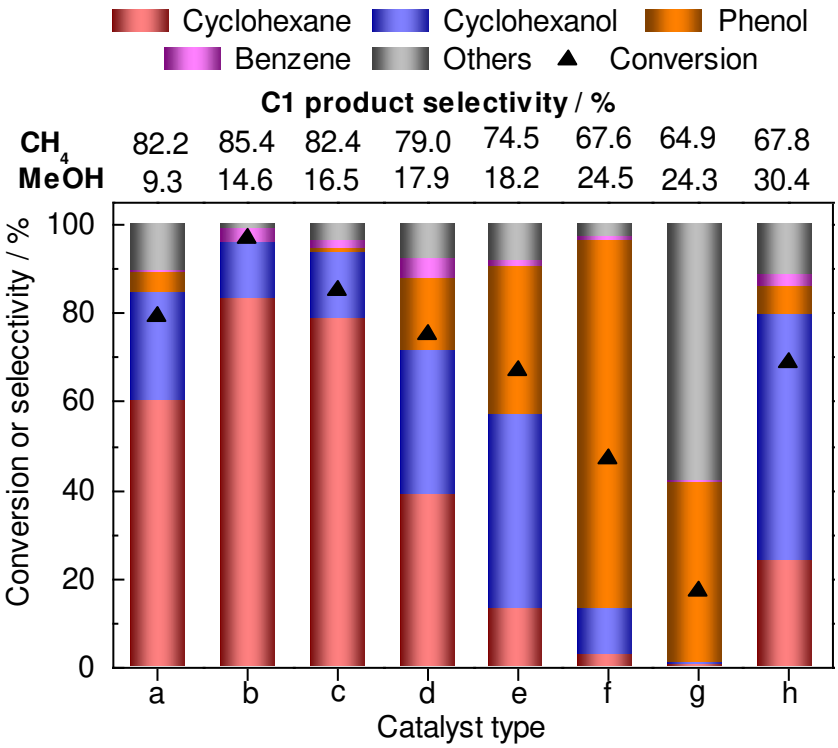

Figure 5 Catalytic performances of Ni–Fe/CNT catalysts with different Ni/Fe atomic ratios. (a) Ni/CNT, (b) Ni_5–Fe_1/CNT, (c) Ni_2–Fe_1/CNT, (d) Ni_1–Fe_1/CNT, (e) Ni_1–Fe_2/CNT, (f) Ni_1–Fe_5/CNT, (g) Fe/CNT, (h) Ni/CNT + Fe/CNT (Ni/Fe = 5:1). Reaction conditions: $WLHSV_{GUA}$= 6.0 h^{-1}, $P(H_2)$=3.0 MPa, H_2/GUA molar ratio = 50, T= 573 K.

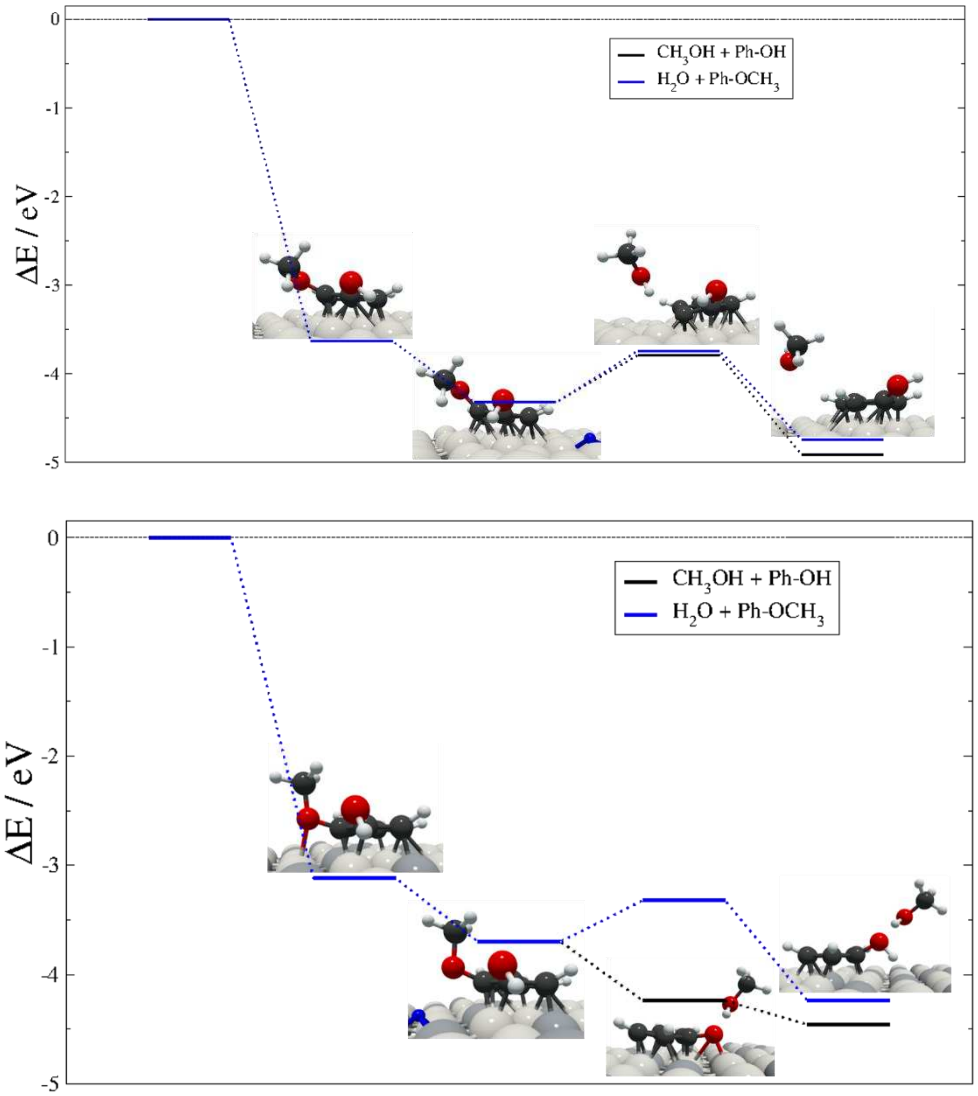

Figure 6 Thermodynamic energy profile for guaiacol reduction on **(A)** pristine Ni(111) and **(B)** $Fe_3Ni(111)$ surfaces. Each state corresponds to a single hydrogenation step leading to CH_3OH + Ph-OH (black line and representation insets) and H_2O + Ph-OCH_3 (blue line). Color scheme: light-grey represents Ni, grey is Fe, dark grey is C, red is O white is H and the co-adsorbed H is represented in blue.

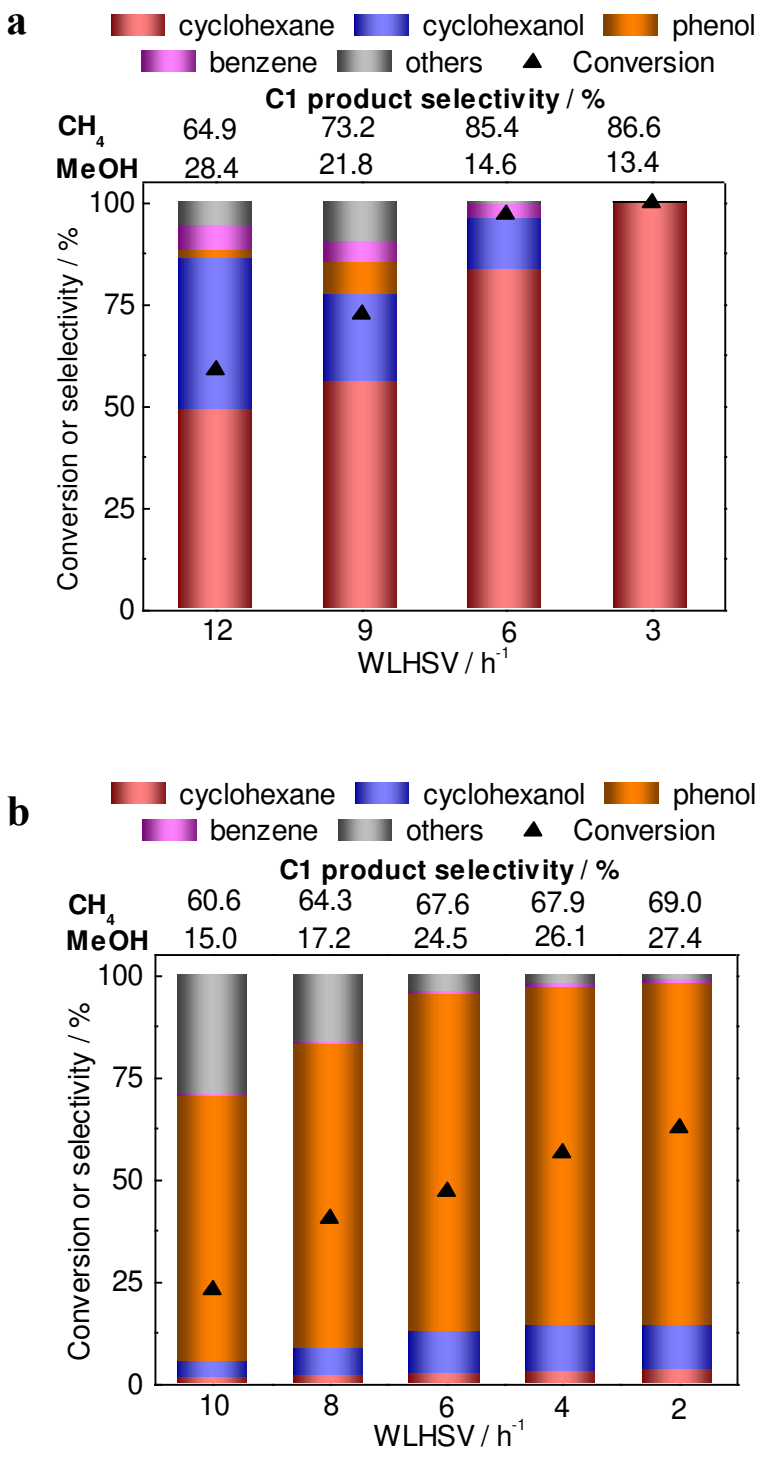

Figure 7 Catalytic performances of catalysts with different WLHSV, P(H_2)=3.0 MPa, H_2/GUA molar ratio = 50, *T*= 573 K, (a) Ni_5Fe_1/CNT, (b) Ni_1Fe_5/CNT.

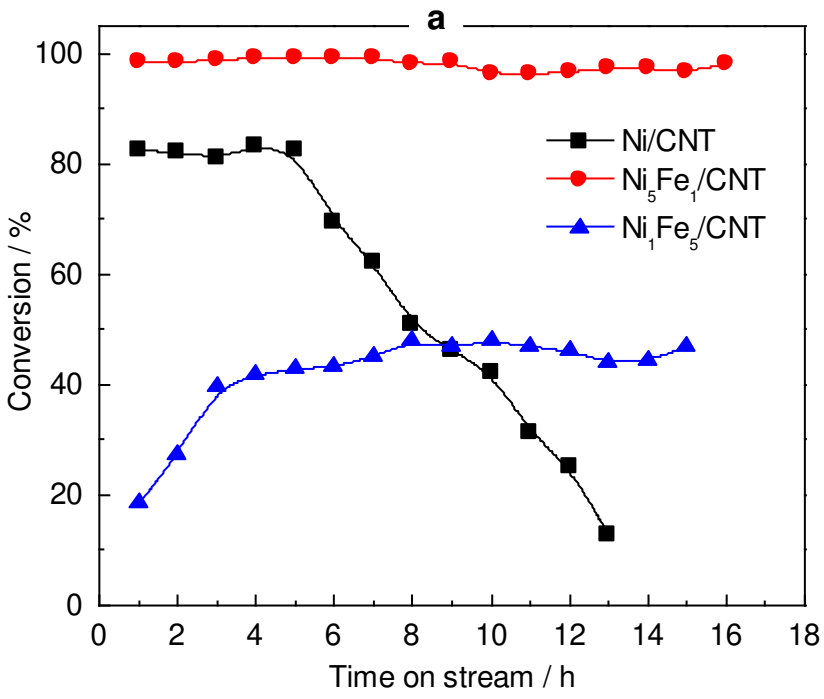

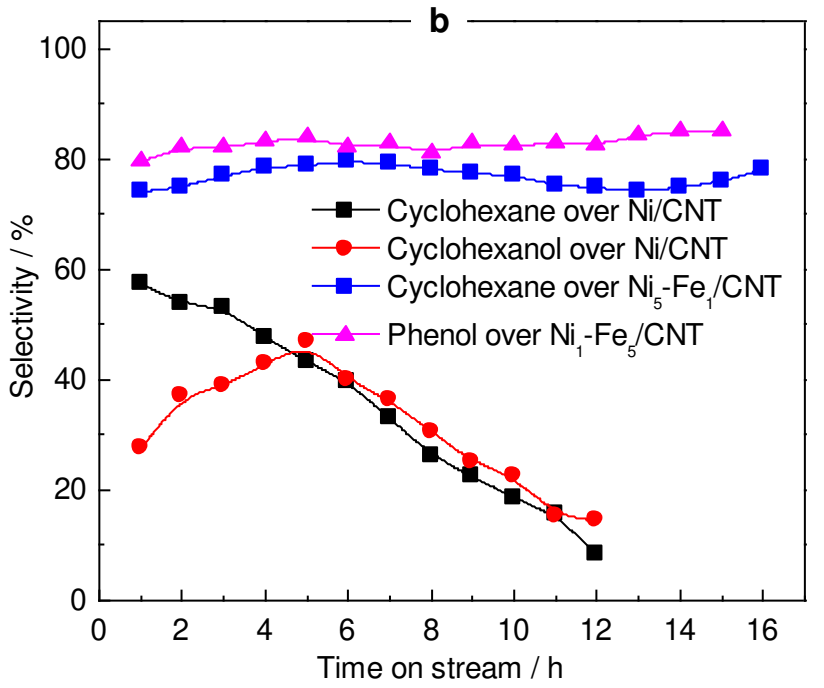

Figure 8 Conversion (a) and selectivity (b) on Ni/CNT, Ni_5–Fe_1/CNT, Ni_1–Fe_5/CNT catalysts as a function of time. Reaction conditions: $WLHSV_{GUA}$= 6.0 h^{-1}, $P(H_2)$ = 3.0 MPa, H_2/GUA molar ratio = 50, T = 573 K.